

Journal Pre-proof

Adaptive multilevel space-time-stepping scheme for transport in heterogeneous porous media (ADM-LTS)

Ludovica Delpopolo Carciopolo, Matteo Cusini, Luca Formaggia, Hadi Hajibeygi

PII: S2590-0552(20)30004-4
DOI: <https://doi.org/10.1016/j.jcp.2020.100052>
Reference: JCPX 100052

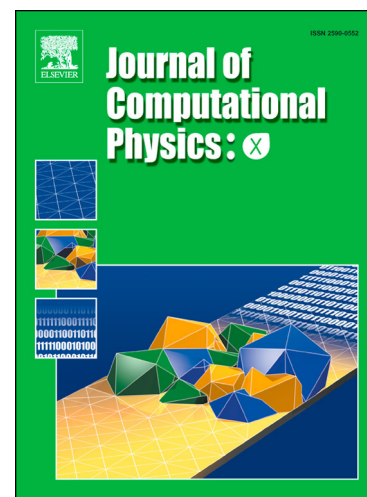
To appear in: *Journal of Computational Physics: X*

Received date: 11 June 2019
Revised date: 10 February 2020
Accepted date: 19 February 2020

Please cite this article as: L. Delpopolo Carciopolo et al., Adaptive multilevel space-time-stepping scheme for transport in heterogeneous porous media (ADM-LTS), *J. Comput. Phys.* (2020), 100052, doi: <https://doi.org/10.1016/j.jcp.2020.100052>.

This is a PDF file of an article that has undergone enhancements after acceptance, such as the addition of a cover page and metadata, and formatting for readability, but it is not yet the definitive version of record. This version will undergo additional copyediting, typesetting and review before it is published in its final form, but we are providing this version to give early visibility of the article. Please note that, during the production process, errors may be discovered which could affect the content, and all legal disclaimers that apply to the journal pertain.

© 2020 Published by Elsevier.



Highlights

- This paper presents the first algebraic dynamic multilevel method with local time-stepping (ADM-LTS) for transport equations.
- The ADM-LTS is integrated within dynamic multiphase flow simulation, with sequentially coupled flow and transport equations.
- The ADM-LTS method allows to associate each spatial resolution level with a corresponding time-step so that time and spatial discretization errors are treated coherently.
- The transport of phase saturation is solved with an adaptive dynamic multilevel grid both in space and in time.
- The combination of the two approaches, i.e. multiscale in space and time, casts an efficient and accurate simulation method for multiphase flow in large-scale porous media.

Adaptive multilevel space-time-stepping scheme for transport in heterogeneous porous media (ADM-LTS)

Ludovica Delpopolo Carciopolo^{a,*}, Matteo Cusini^b, Luca Formaggia^a, Hadi Hajibeygi^c

^a*MOX, Dipartimento di Matematica, Politecnico di Milano, Via Bonardi 9, 20133 Milano, Italy.*

^b*Atmospheric, Earth, & Energy division, Lawrence Livermore National Laboratory, 7000 East Ave., Livermore, CA 94550-9234, United States of America.*

^c*Department of Geoscience and Engineering, Faculty of Civil Engineering and Geosciences, Delft University of Technology, Stevinweg 1, 2628 CN, Delft, the Netherlands.*

Abstract

We present ADM-LTS, an adaptive multilevel space-time-stepping scheme for transport in heterogeneous porous media. At each time step, firstly, the flow (pressure) solution is obtained. Then, the transport equation is solved using the ADM-LTS method, which consists of two stages. In the first stage, an initial solution is obtained by imposing the coarsest space-time grid. This initial solution is then improved, in the second stage, by imposing a space-time adaptive grid on the cells where the solution does not satisfy the desired quality. The quality control is based on error estimators with user-defined threshold values. The time-integration procedure, in which the coarsest-scale solution provides local flux boundary conditions for sub-domains with local time refinement, is strictly mass conservative. In addition, the method employs space-time fine grid cells only at the moving saturation fronts. In order to ensure local mass conservation at all levels, finite-volume restriction operators and unity prolongation operators are developed. Several numerical experiments have been performed to analyze the efficiency and accuracy of the proposed ADM-LTS method for both homogeneous and heterogeneous per-

*Corresponding author.

Email addresses: ludovica.delpopolo@polimi.it (Ludovica Delpopolo Carciopolo), cusini1@llnl.gov (Matteo Cusini), luca.formaggia@polimi.it (Luca Formaggia), H.Hajibeygi@tudelft.nl (Hadi Hajibeygi)

meability fields on two and three dimensional domains. The results show that the method provides accurate solutions, at the same time it maintains the computational efficiency. The ADM-LTS implementation is publicly available at <https://gitlab.com/darsim2simulator>.

Keywords: Local time-stepping strategies, Conservative multirate methods, Algebraic Multilevel methods, Multiphase flow, Porous media

1. Introduction

Simulation of transport in natural porous media is challenging due to the variety of time and length scales involved in the process. In fact, geological formations extend several hundreds of meters whereas physical and chemical phenomena, which are relevant in many applications (e.g., energy and greenhouse gas storage and geo-energy production), occur at much smaller scales (cm and below). Additionally, at the continuum (or Darcy) scale, porous media present highly heterogeneous discrete properties (e.g., permeability) with no separation of scales. This leads to having fast and slow transport processes coexist in one computational domain. Accurate numerical models, thus, require very high resolution grids both in space and time to capture all relevant physics. However, due to the big size of the domains and the large number of simulations for uncertainty reduction [1, 2], field-scale simulations on such high resolution grids are impractical.

The global system complexity cannot be reduced by upscaling approaches, as the heterogeneous properties often times do not entail clear separation of scales [3]. Alternatively, one can map scalable part of the solution (e.g. pressure) in coarser spatial resolutions, as in the multiscale methods [4, 5, 6, 7, 8]. For the transport (e.g. saturation) equation, due to its local nature, Adaptive Mesh Refinement (AMR) schemes provide a promising framework for the reduction of the computational complexity [9, 10]. Both approaches address resolution challenges in space only, which can be integrated into an operator-based strategy by the Algebraic Dynamic Multilevel (ADM) method [11, 12].

ADM maps the spatial fine-scale system into a dynamic multilevel system by using sequences of local operators (restriction and prolongation). It can be applied to coupled flow-transport, or only transport equation. In addition to explicit and implicit time integration schemes, both sequential and fully-implicit coupling strategies can be treated in a straightforward manner. The

30 focus of the present study is on the transport equation, which is sequentially
31 coupled with the pressure and velocity solver at each time step.

32 Similar to AMR, ADM develops an adaptive spatial-grid stepping scheme.
33 In contrast to AMR, however, ADM is applicable to heterogeneous systems
34 without dependency on upscaling parameters.

35 Although important, spatial grid is only part of the full transport simulation
36 advancement. To further advance the overall simulation efficiency, one may
37 need to take large time step sizes. However, the excessive numerical disper-
38 sion introduced by the use of large time steps can significantly impact the
39 accuracy of the solution, e.g., by smearing the advancing saturation front. It
40 is therefore crucially important to, not only allow for large time step sizes,
41 but also to control the accuracy by resolving the sharp fronts using smaller
42 time steps. Such a development is made possible—for static spatial grids—by
43 Local Time Stepping (LTS) or multirate methods [13]. Recent LTS methods
44 allow for self-adjusting time-stepping strategies based on a posteriori error
45 estimator [14] in a strictly conservative implicit time integration framework
46 [15]. The LTS for conservative transport simulation on fine-scale spatial grid
47 has been also successfully integrated with the pressure solver of the multi-
48 scale finite volume method [16]. This idea was also followed to develop an
49 explicit LTS scheme [17]. Note that all of these mentioned methods depend
50 on a given static single-level spatial grid for transport.

51 Of particular interest is to develop an adaptive space-time stepping scheme
52 for transport simulation. This development would allow not only to adjust
53 the spatial, but also temporal grid in order to achieve the optimum efficient
54 and accurate transport solutions.

55 In this paper, the adaptive space-time stepping scheme (ADM-LTS) is
56 devised. This new development makes it possible to march adaptively both
57 in space and time (with an arbitrary number of levels) to obtain accurate
58 and efficient solutions for complex transport in heterogeneous porous media.
59 Additionally, the proposed ADM-LTS method preserves mass conservation,
60 even though it takes different time step sizes in different subsets of the do-
61 main. This is made possible by obtaining an initial solution estimator on the
62 coarsest space-time grid, and impose it as Neumann (fixed flux) boundary
63 condition to local regions with smaller space-time steps.

64 Note that the ADM-LTS is developed for the transport equation, within
65 the coupled flow-transport multiphase simulation. In particular, it is empha-
66 sized that the pressure equation solution is assumed to be available by any
67 advanced solver, which stays out of the scope of this paper. Once the pres-

68 sure and velocity fields are obtained, ADM-LTS is imposed on the transport
 69 equation, with adaptive space-time grid based on space-time error estima-
 70 tors. As a consequence, the method is able to use a fine-grid resolution (in
 71 space and time) only at the location of the moving saturation fronts. More
 72 precisely, the method first applies a global time step on the coarsest possi-
 73 ble grid resolution. Then, it defines a multilevel grid resolution on the basis
 74 on the error estimators. On this new grid, the solution is recomputed with
 75 smaller time steps only in a fraction of the domain.

76 ADM-LTS is different, yet complementary, to other advanced methods
 77 for transport equation, specially the Adaptive Implicit Method (AIM) [18,
 78 19, 20]. AIM develops an adaptive implicit-explicit time-integration scheme,
 79 but takes the same space-time grids everywhere. ADM-LTS, on the other
 80 hand, is developed to allow different space and time step sizes in a domain,
 81 irrespective of the choice of the time-integration scheme.

82 The ADM-LTS method is applied to homogeneous and heterogeneous
 83 2D and 3D test cases including complex nonlinear transport physics (i.e.,
 84 gravitational forces and capillarity heterogeneity). Systematic studies of the
 85 performance (i.e., accuracy and system complexity) are presented. Numerical
 86 test cases show that the ADM-LTS approach provides an accurate solution
 87 reducing the number of active cells both in space and in time.

88 The paper is organized as follows. The equations describing multiphase
 89 flow in porous media are presented in section 2 along with the fine-scale
 90 discrete systems for transport equation. The ADM-LTS method is explained
 91 in detail in section 3 whereas numerical experiments are presented in section
 92 4. Finally, conclusions are provided in section 5.

93 2. Sequential-implicit simulation

94 Mass conservation equations for the flow of N_p incompressible phases in
 95 a d -dimensional porous domain $\Omega \subset \mathbb{R}^d$ read

$$\frac{\partial}{\partial t} (\phi \rho_\alpha S_\alpha) + \nabla \cdot (\rho_\alpha \mathbf{u}_\alpha) = q_\alpha \quad \forall \alpha \in \{1, \dots, N_p\}. \quad (1)$$

96 Here, S_α , ρ_α and q_α are the α -phase saturation, density and source term (i.e.,
 97 wells). The Darcy velocity for α -phase can be written as

$$\mathbf{u}_\alpha = -\mathbf{K} \lambda_\alpha (\nabla p_\alpha + \rho_\alpha g \nabla z) \quad \forall \alpha \in \{1, \dots, N_p\}. \quad (2)$$

98 Here, the phase mobility is denoted by λ_α , and $\lambda_\alpha = k_{r\alpha}/\mu_\alpha$ holds, where
 99 $k_{r\alpha}$ and μ_α are the phase relative permeability and viscosity, respectively.
 100 Furthermore, \mathbf{K} is the rock absolute permeability (defined at discrete fine-
 101 scale resolution). Additionally, p_α are the phase pressures, which are related
 102 to the capillary pressure P_c as

$$p_\alpha - p_\beta = (1 - \delta_{\alpha,\beta})P_{c_{\alpha,\beta}} \quad \forall \alpha, \beta \in \{1, \dots, N_p\}. \quad (3)$$

103 Here, $\delta_{\alpha,\beta}$ is the Kronecker delta, which is equal to 1 if $\alpha = \beta$ and 0 otherwise,
 104 while $P_{c_{\alpha,\beta}}$ is a nonlinear function of wetting phase saturation. Note that
 105 the constraint $\sum_{\alpha=1}^{N_p} S_\alpha = 1$ allows for eliminating one of the unknowns.
 106 Assuming incompressible fluids and rock, in a two-phase system one can use
 107 the non wetting (nw) pressure and the wetting (w) saturation as primary
 108 variables [21, 22]. We will then set $p = p_{nw}$, $S = S_w$ and define a total
 109 velocity as

$$\mathbf{u}_t = \mathbf{u}_{nw} + \mathbf{u}_w. \quad (4)$$

110 Sequential-implicit simulation requires a decoupled pressure-saturation sets
 111 of equations. The equation for pressure is obtained by combining the mass-
 112 balance equations, to have

$$\nabla \cdot \mathbf{u}_t = \frac{q_w}{\rho_w} + \frac{q_{nw}}{\rho_{nw}} \quad \text{in } \Omega, \quad (5)$$

113 where the total velocity is expressed as

$$\mathbf{u}_t = \mathbf{K} \left(-\lambda_t \nabla p + \lambda_w \nabla P_c - (\lambda_w \rho_w + \lambda_{nw} \rho_{nw}) g \nabla z \right). \quad (6)$$

114 On the other hand, the (wetting-phase) saturation equation is re-written by
 115 introducing the fractional flow function $f_w = \lambda_w/\lambda_t$, thus obtaining

$$\frac{\partial(\phi S)}{\partial t} + \nabla \cdot \left\{ \mathbf{K} f_w \lambda_{nw} (\nabla P_c + (\rho_{nw} - \rho_w) g \nabla z) + f_w \mathbf{u}_t \right\} = \frac{q_w}{\rho_w} \quad \text{in } \Omega. \quad (7)$$

116 Equations (5), (6) and (7) are coupled by the total velocity, the (nonlin-
 117 ear) phase relative permeability $k_{r\alpha}$ and the capillary pressure P_c .

118 Sequential implicit simulation (SIM) consists of decoupling the pressure
 119 and transport equations at numerical level, and solving each of them implic-
 120 itly in time. Given the state at a current time t^n , the solution at time t^{n+1}
 121 is found by first solving Eq. (5), freezing all saturation dependencies, i.e.,

$$-\nabla \cdot (\mathbf{K} \lambda_t^n \nabla p^{n+1}) = q_t - \nabla \cdot (\mathbf{K} (\lambda_w^n \nabla P_c^n - (\lambda_w^n \rho_w + \lambda_{nw}^n \rho_{nw}) g \nabla z)), \quad (8)$$

122 where $q_t = q_w/\rho_w + q_{nw}/\rho_{nw}$. Then, the total velocity is computed as

$$\mathbf{u}_t^{n+1} = -\mathbf{K} \left(\lambda_t^n \nabla p^{n+1} - \lambda_w^n \nabla P_c^n + (\lambda_w^n \rho_w + \lambda_{nw}^n \rho_{nw}) g \nabla z \right). \quad (9)$$

123 Finally the transport equation is solved, i.e.,

$$\begin{aligned} & \phi \frac{S^{n+1} - S^n}{\Delta t} + \\ & \nabla \cdot (\mathbf{K} f_w^{n+1} \lambda_{nw}^{n+1} (\nabla P_c^{n+1} + (\rho_{nw} - \rho_w) g \nabla z) + f_w^{n+1} \mathbf{u}_t^{n+1}) - \frac{q_w^{n+1}}{\rho_w} = 0. \end{aligned} \quad (10)$$

124 The saturation equation is a nonlinear function. Thus, we employ a
125 Newton-Raphson's method for Eq. (10), which leads to a sequence of systems
126 of the form $\mathbf{J}^\nu \delta \mathbf{x}^{\nu+1} = -\mathbf{r}^\nu$. Here, $\delta \mathbf{x}$ is the vector of increment for saturation,
127 \mathbf{J} is the Jacobian matrix, \mathbf{r} is the residual, and ν the iteration index.

128 For each cell K , one can write the residual as

$$\mathbf{r}_K^{n+1} = \phi(S_K^{n+1} - S_K^n) - \frac{1}{|K|} \sum_{e_{KL} \in \mathcal{E}_K} e_{KL} F_{KL}^{n+1} - \frac{q_w^{n+1}}{\rho_w} = 0. \quad (11)$$

129 Here, $|K|$ is the volume of element K , e_{KL} the area of the interface between
130 cells K and L and \mathcal{E}_K the set of faces e of the element K . Finally, F_{KL}^{n+1} is a
131 numerical flux, which can be decomposed into three parts to have a separate
132 treatment of each mobility term. Namely,

$$F_{KL}^{n+1} = (V_{KL}^{n+1} + G_{KL}^{n+1} + C_{KL}^{n+1}), \quad (12)$$

133 where V_{KL}^{n+1} , G_{KL}^{n+1} and C_{KL}^{n+1} are the viscous, buoyancy and capillary nu-
134 merical fluxes, respectively. In the viscous numerical flux, the mobility is
135 calculated using an upwind method based on the sign of the total velocity,
136 i.e.,

$$V_{KL}^{n+1} = \begin{cases} \Delta t f_w(S_U^{n+1}) u_{TKL} & \text{if } u_{TKL} > 0 \\ \Delta t f_w(S_D^{n+1}) u_{TKL} & \text{otherwise.} \end{cases} \quad (13)$$

137 Here, S_U and S_D denote the upstream and downstream saturation values,
138 respectively. In the gravity numerical flux, the mobility is computed based
139 on the density differences, i.e.,

$$G_{KL}^{n+1} = \begin{cases} \Delta t T_{KL} f_w(S_U^{n+1}) \lambda_{nw}(S_U^{n+1}) \Delta \rho g (z_L - z_K) & \text{if } \Delta \rho g (z_L - z_K) > 0 \\ \Delta t T_{KL} f_w(S_D^{n+1}) \lambda_{nw}(S_D^{n+1}) \Delta \rho g (z_L - z_K) & \text{otherwise.} \end{cases} \quad (14)$$

140 Here, $\Delta\rho = (\rho_{nw} - \rho_w)$, and T_{KL} is the interface normalized transmissibility
 141 (normalized by the grid cell cross-section area), which is computed as the
 142 harmonic average of the neighboring cell parameters, i.e.,

$$T_{KL} = \left(\frac{d_{Ke}}{\mathbf{K}_K} + \frac{d_{eL}}{\mathbf{K}_L} \right)^{-1}, \quad (15)$$

143 where d_{Ke} and d_{eL} are the distances between the face e_{KL} and the centers of
 144 cells K and L , respectively. Finally, the capillary numerical flux is calculated
 145 as

$$C_{KL}^{n+1} = \begin{cases} \Delta t T_{KL} f_w(S_U^{n+1}) \lambda_{nw}(S_U^{n+1}) (P_{c_L}^{n+1} - P_{c_K}^{n+1}) & \text{if } u_{T_{KL}} > 0 \\ \Delta t T_{KL} f_w(S_D^{n+1}) \lambda_{nw}(S_D^{n+1}) (P_{c_L}^{n+1} - P_{c_K}^{n+1}) & \text{otherwise.} \end{cases} \quad (16)$$

146 The quality of the solution of Eq. (10) is highly influenced by the res-
 147 olution of the spatial and time discretization scheme. The objective of this
 148 work is to develop a space-time multilevel adaptive method (ADM-LTS) to
 149 solve Eq. (10) accurately and efficiently.

150 3. ADM-LTS method

151 In this section, first, the original ADM method [11] is reviewed, then, the
 152 newly proposed ADM-LTS algorithm is presented in detail.

153 3.1. The ADM method

154 The ADM method is employed to reduce the computational cost associ-
 155 ated with the solution of the linear system arising from the linearized problem
 156 of Eq. (10).

157 Let us consider a domain discretized with a high resolution grid which is
 158 assumed to be fine enough to capture all relevant physics and to honor the
 159 heterogeneous distribution of the geological properties. Given this fine-scale
 160 discretization, a hierarchy of n_l nested coarse grids is constructed. Each grid
 161 is formed by $N_l = N_{lx} \times N_{ly} \times N_{lz}$ grid cells, where l is the resolution index
 162 and $l = 0$ represents the fine grid resolution.

163 The set of all grid cells belonging to resolution level l is called Π^l . At each
 164 time step ADM defines a multilevel grid by combining grid cells belonging to
 165 the hierarchy of grids previously defined. Given a multilevel ADM grid, let
 166 us define Ω^l as the set of grid cells belonging to all levels from 0 to l which

167 are present in the ADM grid. Additionally, it is convenient to define the set
 168 Γ^l as $\Gamma^l = \Omega^l \cap \Pi^l$.

169 Given an ADM grid formed by the set of grid cells Ω^l , ADM assumes
 170 that the fine scale solution can be approximated by employing a sequence of
 171 prolongation operators, i.e.

$$\delta \mathbf{x}_f \approx \delta \mathbf{x}' = \hat{\mathbf{P}}_0^1 \dots \hat{\mathbf{P}}_{l-1}^l \delta \mathbf{x}^{ADM}. \quad (17)$$

172 Here, operator $\hat{\mathbf{P}}_{i-1}^i$ interpolates the solution at level i to the finer resolution
 173 level $(i-1)$ and $\delta \mathbf{x}^{ADM}$ is the vector of increment for the ADM solution on
 174 the adaptive multilevel grid. The fine-scale Jacobian system is mapped to
 175 the ADM grid by

$$\hat{\mathbf{R}}_l^{l-1} \dots \hat{\mathbf{R}}_1^0 \hat{\mathbf{J}} \hat{\mathbf{P}}_0^1 \dots \hat{\mathbf{P}}_{l-1}^l \delta \mathbf{x}^{ADM} = -\hat{\mathbf{R}}_l^{l-1} \dots \hat{\mathbf{R}}_1^0 \mathbf{r}_f, \quad (18)$$

176 where $\hat{\mathbf{R}}_i^{i-1}$ is the restriction operator which maps the solution from resolution
 177 at level i to coarser level $(i-1)$. In order to ensure mass conservation at all
 178 level, a finite volume restriction operator is considered [5]. Thus, the entry
 179 (i, j) of a restriction operator reads

$$\hat{\mathbf{R}}_i^{i-1}(i, j) = \begin{cases} 1 & \text{if cell } i \in \Gamma^i \text{ and cell } j \in \Gamma^{i-1}, \\ \delta_{ij} & \text{otherwise.} \end{cases} \quad (19)$$

180 Additionally, constant interpolation is considered for saturation,

$$\hat{\mathbf{P}}_{l-1}^l = \left(\hat{\mathbf{R}}_l^{l-1} \right)^T. \quad (20)$$

181 Consequently, no solution step is required to compute the prolongation op-
 182 erator.

183 3.2. ADM method with local time-stepping (ADM-LTS)

184 At each time step n , having solved the pressure equation and computed
 185 the total velocity field, we address the transport equation employing the
 186 ADM-LTS algorithm.

187 First, Eq. (18) is solved with time step Δt over the whole domain on
 188 the coarsest grid resolution (l_{max}) formed by cells belonging to $\Pi^{l_{max}}$ and
 189 limiting refinement only around the wells. Then, based on the coarse solution
 190 obtained, the proper ADM grid resolution is chosen according to a front-
 191 tracking criterion. Two alternative front-tracking strategies are considered
 192 in this work:

- 193 • a criterion based on the saturation difference between neighboring cells.
 194 A cell i belonging to level l is refined whenever the saturation difference,
 195 as defined in [11], between i and one of its neighbors exceeds a user-
 196 defined tolerance ϵ_x .
- 197 • a time-dependent criterion combined with the previous one to deter-
 198 mine whether cells belonging to Π^0 should stay fine. Let us define
 199 $\psi_S = S^{n+1} - S^n$. A fine cell i is kept at the fine resolution only
 200 if $\psi_{S_i} > \epsilon_t$, where ϵ_t is a user-defined tolerance. A similar time-
 201 based coarsening criterion has successfully been used in the literature
 202 for channelized heterogeneous problems where stationary gradients are
 203 present [23].

204 Once the ADM grid resolution has been defined, the solution is recom-
 205 puted for all cells belonging to $\Omega^{l_{max}-1}$ with a time step $\Delta t_{l_{max}-1} = \Delta t/\eta$
 206 by imposing local boundary conditions as described in detail in the following
 207 subsection. Here η is the time refinement ratio. Then, the same operation is
 208 repeated for all resolution levels l until $l = 0$ has been reached. Thus, each
 209 resolution level l (formed by the set of grid blocks Ω^l) is solved with a time
 210 step $\Delta t_l = \Delta t_{l+1}/\eta$. For the finest level ($l = 0$) ADM-LTS only recomputes
 211 the solution, with time step $\Delta t_0 = \Delta t/\eta^{l_{max}}$, for a subset, defined Ω_A^0 , of the
 212 cells belonging to Ω^0 . In fact, only fine cells for which $\psi_S = S^{n+\Delta t_1} - S^n > \epsilon_t$
 213 are part of the set Ω_A^0 .

214 The method advances in time for the active cells in Ω_A^0 until they reach
 215 $t = t^n + \Delta t_1$. Once they are synchronized, cells in Ω^1 advance in time. At
 216 this point, a new set of cells Ω_A^0 is selected and these cells are advanced by
 217 Δt_1 performing $\eta \Delta t_0$ time steps. Once all cells in Ω^1 have reached time
 218 $t = t^n + \Delta t_2$ another time step Δt_2 can be performed for all cells belonging
 219 to Ω^2 . This is a recursive procedure which is performed for all levels until all
 220 cells have reached time $t^{n+1} = t^n + \Delta t$.

221 Figure 1 illustrates a schematic overview of the ADM-LTS method where
 222 η and l_{max} are both taken equal to 2. Figure 2 shows an example of the
 223 ADM grid at each step and the refining area. At the global time step Δt , the
 224 solution is computed on the coarsest resolution l_{max} . At the intermediate time
 225 step the ADM grid resolution is defined and the solution is recomputed with
 226 the intermediate time step everywhere except at the coarsest region (middle
 227 figure). At the end, the method checks the errors and defines the set of
 228 active cells Ω_A^0 (pink region on the right), the solution is recomputed with the
 229 smallest time step. Note that the solution at each local time step is performed

230 at a different space-time resolution. Furthermore, all cells belonging to the
 231 coarsest level march with the biggest time step size. On the other hand, the
 232 saturation at cells in Ω_A^0 (i.e., where higher resolution is needed) naturally
 233 advance with smaller time step sizes.

234 We remark that the quality of the solution and the efficiency of the ADM-
 235 LTS algorithm will be significantly affected by the choice of the user-defined
 236 tolerances ϵ_x and ϵ_t . Even though, a general strategy cannot be defined,
 237 simple analytical solutions (e.g., Buckley-Leverett) can be used to estimate
 238 the value of the saturation front and deduce effective values for the toler-
 239 ances that will have to be determined to obtain the desired trade-off between
 240 accuracy and efficiency.

241 3.2.1. Local systems and local boundary conditions

242 For each resolution level l , the set of grid cells Ω^l is solved with the
 243 corresponding time step $\Delta t_l = \frac{\Delta t}{\eta^{(l_{max}-l)}}$. The number of active cells contained
 244 by Ω_l is denoted by N_A^l .

245 When solving for the cells belonging to Ω^l , the numerical flux at the inter-
 246 face between two cells K and L such that $K \in \Omega^l \wedge L \in \Gamma^{l+1}$ is approximated
 247 by

$$F_{KL}^{n+\beta(i)} = \frac{F_{KL}^{n+\gamma(j)}}{\eta} \quad (21)$$

248 where

$$\beta(i) = \frac{i}{\eta^{(l_{max}-l)}}, \quad i = \{1 \dots \eta^{(l_{max}-l)}\} \quad (22)$$

$$\gamma(j) = \frac{j}{\eta^{(l_{max}-l-1)}}, \quad j = \{1 \dots \eta^{(l_{max}-l-1)}\}. \quad (23)$$

250 Thus, Eq. (11) can be modified to account for the presence of different time
 251 levels as

$$\begin{aligned} r_K^{n+\beta(i)} &= \phi(S_K^{n+\beta(i)} - S_K^{n+\beta(i)-1}) \\ &\quad - \frac{1}{|K|} \sum_{e_{KL} \in \mathcal{E}_{KA}} e_{KL} F_{KL}^{n+\beta(i)} - \frac{q_w^{n+\beta(i)}}{\rho_w} - \frac{1}{|K|} \sum_{e_{KL} \in \mathcal{E}_{KL}} e_{KL} \frac{F_{KL}^{n+\gamma(j)}}{\eta}. \end{aligned} \quad (24)$$

252 Here, \mathcal{E}_{KA} is the set of interface fluxes exchanged between two cells K
 253 and L both belonging to Ω^l . Additionally, \mathcal{E}_{KL} is the set of fluxes at the

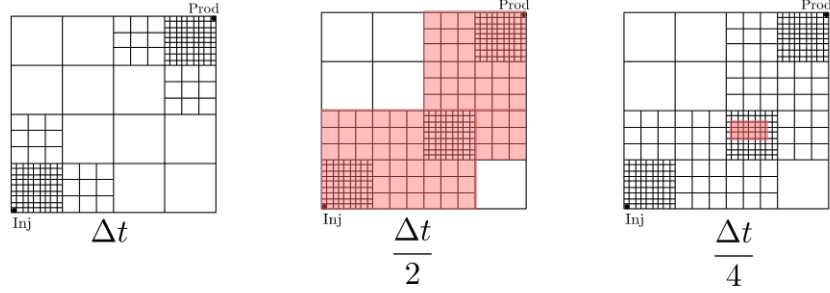


Figure 2: Example of ADM grid and active regions for the refinement time steps with $\eta = 2$ and $l_{max} = 2$.

254 interface between two cells K and L where $K \in \Omega^l$ and $L \in \Gamma^{l+1}$. Note that,
 255 for $l = 0$ the residual for the active cells is the same described in Eq. (11),
 256 but \mathcal{E}_{KL} would be the set of fluxes at the interface between Ω_A^0 and $\Omega^1 \setminus \Omega_A^0$.

257 We remark that, for each level l , the linear system to be solved has size
 258 $N_A^l \times N_A^l$, which is significantly smaller than the full fine-scale system. At
 259 each time step, only a sub-set of the cells of each level l is restricted and
 260 prolonged.

261 The following section presents a study of the performance of the ADM-
 262 LTS method for various 2D and 3D test cases involving different fluid physics.

263 4. Numerical results

264 The performance of the newly developed ADM-LTS strategy is thoroughly
 265 investigated for several challenging test cases. For all the cases presented,
 266 quadratic relative permeability curves are considered. Gravitational and
 267 capillary forces are only considered in test cases 2 and 7, respectively. Fur-
 268 thermore, all errors are computed with respect to a reference solution, ob-
 269 tained by employing a high resolution discretization both in space and in
 270 time.

271 4.1. Test case 1: 2D homogeneous reservoir

272 The first test case is a 100×100 [m²] homogeneous reservoir, with isotropic
 273 permeability of 5×10^{-15} [m²]. A pressure-constrained wetting-phase injector
 274 well is positioned in the bottom-left corner of the domain with a pressure
 275 $p_{inj} = 10^8$ [Pa], whereas a production well is present in the top-right corner
 276 with a relative pressure of $p_{prod} = 0$ [Pa]. The phase viscosity values are

277 $\mu_w = 10^{-3}$ [Pa · s] and $\mu_{nw} = 10^{-2}$ [Pa · s] for the wetting and non wetting
 278 phase, respectively. The final simulated time is 600 [days] after injection has
 279 started.

280 A fine-scale grid with 99×99 cells is imposed on the domain. ADM-LTS
 281 employs, a time refining ratio $\eta = 2$ and a space coarsening ratio equal to 3 in
 282 all directions. The user-defined tolerances for the coarsening and refinement
 283 criteria are $\epsilon_x = 0.07$ and $\epsilon_t = 5 \times 10^{-2}$.

284 Simulations are run employing three different global time step sizes: 5,
 285 10 and 20 days. Figure 3 reports the CFL values at time $t = 500$ days for
 286 the three different time steps for fine-scale in space simulations.

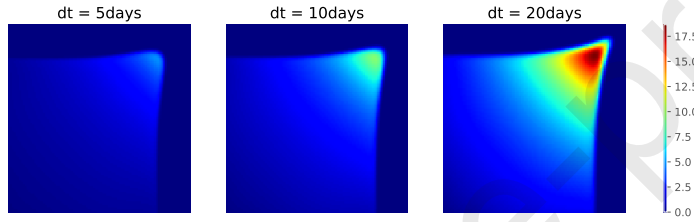


Figure 3: Test case 1 [99×99] - CFL values for different global time steps at time $t = 500$ days.

287 Figure 4 shows a comparison of the ADM-LTS solution with the reference
 288 solution (on the left) at time $t = 500$ [days] using three different sizes of the
 global time steps.

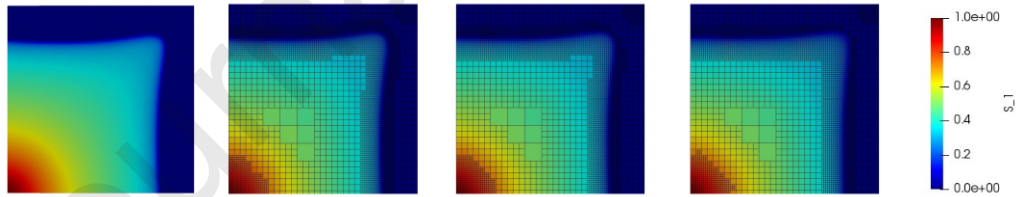


Figure 4: Test case 1 [99×99] - Reference solution (first column) and ADM-LTS solution using a global time step size: $\Delta t = 5, 10$ and 20 [days] at time $t = 500$ days for the second, third and fourth column, respectively.

289 Figure 5 reports the error for the saturation at time $t = 500$ days between
 290 a reference solution and the ADM method with fine time steps (first column)
 291 with the LTS approach (second column) and with the coarse time steps (third
 292 column).

293 column) for the three different time steps sizes $\Delta t = 5$ (first row), $\Delta t = 10$
 294 (second row) and $\Delta t = 20$ (third row). In all cases the AMD-LTS approach
 295 improves the errors with respect to the coarse time step approach.

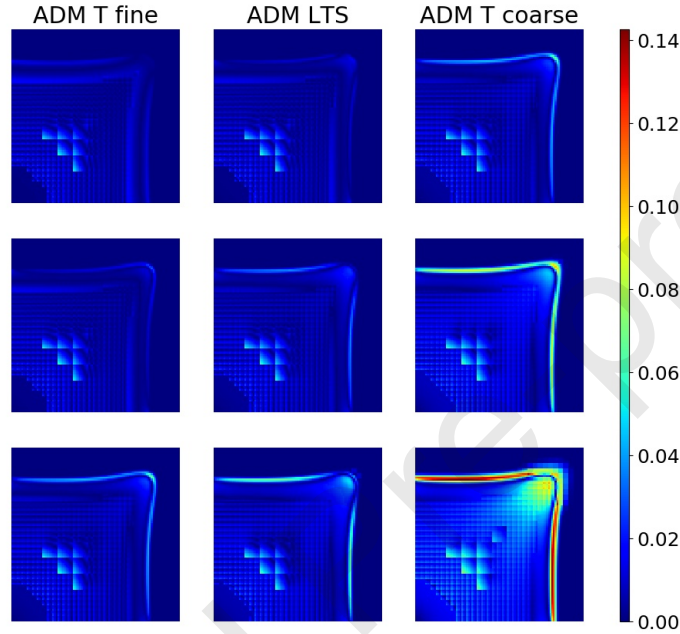


Figure 5: Test case 1 $[99 \times 99]$ - Saturation errors for the ADM method with fine time steps (first column), ADM-LTS method (second column) and ADM coarse time steps method (third column) for the three different global time step sizes.

296 The complexity of the algorithm is shown in Fig. 6. In particular, each
 297 column represents the total amount of active cells multiplied by the number of
 298 Newton iterations involved to compute the solution, for the three approaches
 299 and for the three different global time step sizes. Note that, to obtain the
 300 solution at time $t=600$ [days], 120, 60 and 30 global time steps have been
 301 performed using the three analyzed time steps. We remark that the errors
 302 obtained by employing the original ADM method with a fine time step are
 303 comparable to those obtained with ADM-LTS in terms of accuracy.

304 Figure 7 shows the complexity of a single global time step. For the ADM
 305 method with fine time steps, the local steps are just the small steps applied

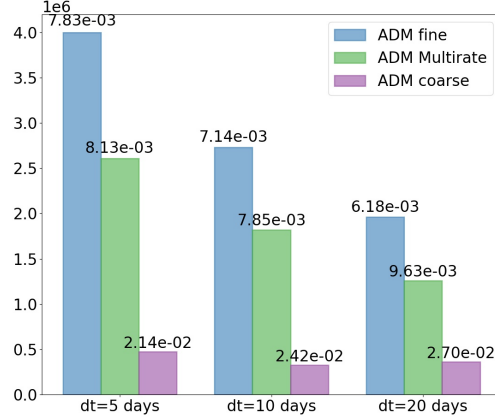


Figure 6: Test case 1 $[99 \times 99]$ - Total amount of active cells multiplied by number of Newton iterations for the three different time step sizes. On the top of each bar the mean in time of the averaged absolute difference respect to the reference solution for the saturation is displayed $E_s = \text{mean}|S(t_f) - S_{ref}(t_f)|$ where t_f is the final time 600 days.

306 at the whole domain. At the end of the local steps both the ADM-LTS
 307 method and the ADM fine step method reach the same time. For the ADM-
 308 LTS method, local step 1 indicates the global step on the coarsest grid, step 2
 309 and 5 are the intermediate time steps performed on level 0 and 1 of the ADM
 310 grid, and the other local steps are the small time steps for the active cells
 311 detected by the error estimator in time. In particular, we can notice that
 312 the intermediate time steps have almost the same complexity of the small
 313 time steps of the ADM fine method, even if the size of the time step is two
 314 times bigger with almost the same number of active cells. This is due to the
 315 improvement of the initial guess for the Newton loop. In the intermediate
 316 time steps we use as initial guess a linear combination of the solution of the
 317 previous time t^n and the solution obtained on the coarsest grid at the new
 318 global time t^{n+1} . In the small time steps is not necessary to perform this
 319 technique since a small step is used to advance in time.

320 The same test case is analyzed after performing a 2×2 refinement of the
 321 space fine-scale grid. In order to obtain a reasonable solution, using a global
 322 Δt equal to 20 [days], we need to compute more local time steps inside the
 323 global one, so a refining ratio equal to 4 has been taken into account.

324 Figure 8 reports the complexity for the entire simulation using ADM-

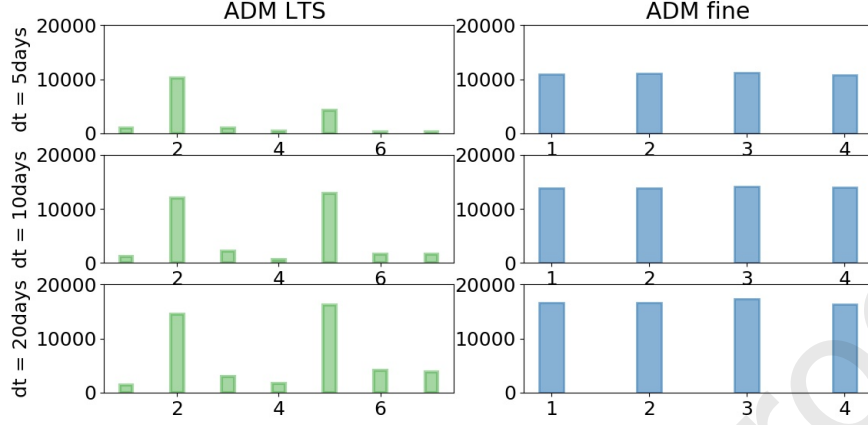


Figure 7: Test case 1 $[99 \times 99]$ - Computational complexity history at each local times step within a global step. The computation complexity is the number of active cells multiplied by the number of Newton iterations.

325 LTS method and the ADM with fine time steps. To obtain the solution at
 326 final time $t = 600$ [days] with a global time step equal to 20 days, the same
 327 number of global time step are involved (30 time steps in total). Of course
 328 the number of local time step for both the LTS method and the fine time
 329 steps approach has increased; but the ratio between active cells and total
 330 cells decreases.

331 Figure 9 shows the averaged number of active cells times the number of
 332 Newton iterations for each local time step within a global time step.

333 In Figure 10 we can see that the ADM-LTS approach reduces the errors
 334 obtained using a coarse grid in time.

335 4.2. Test case 2: 3D homogeneous reservoir

336 A 3D $108 \times 108 \times 108$ [m³] homogeneous reservoir is considered in this
 337 test case. The domain is discretized, at the fine-scale, with a $54 \times 54 \times 54$
 338 Cartesian grid for a total of 157464 cells. The physical parameters are the
 339 same of the first test case. The size of the global steps is equal to 125 days.
 340 The simulation ends after 70 global steps. The tolerances for the coarsening
 341 criteria in space and time are set to be $\epsilon_x = 0.2$ and $\epsilon_t = 5 \times 10^{-2}$.

342 Figure 11 reports the saturation maps at two different simulation times
 343 (on the top) neglecting the gravity effects. It also displays the set of active
 344 cells Ω_A^0 at time $t = 1500$ days (left, bottom) and a section of the solution at

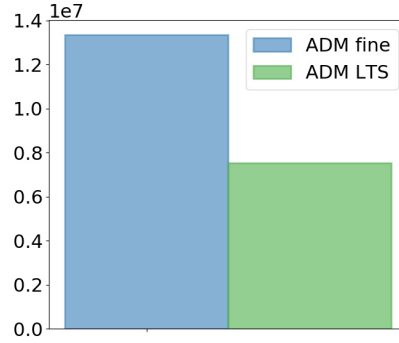


Figure 8: Test case 1 [198×198] - Total amount of active cells multiplied by number of Newton iterations for the ADM with fine time steps and the ADM LTS method.

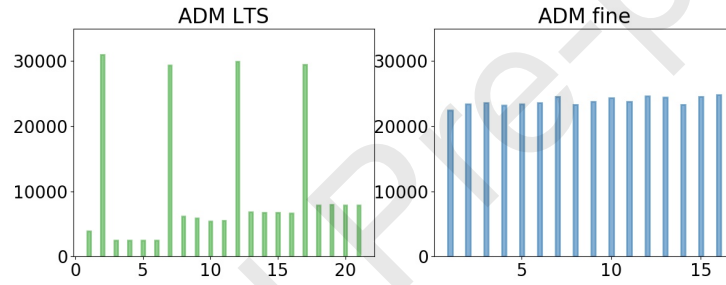


Figure 9: Test case 1 [198×198] - Computational complexity history at each local times step within a global step. The computation complexity is the number of active cells multiplied by the number of Newton iterations.

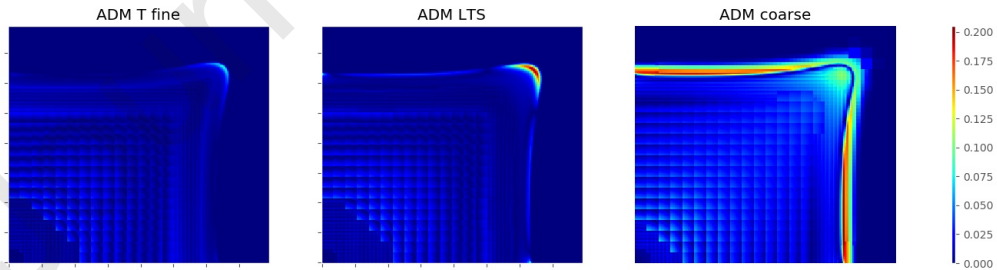


Figure 10: Test case 1 [198×198] - Saturation errors at time $t = 540$ [days] for the ADM method with fine grid in time (left), ADM-LTS method (center) and the ADM method with coarse grid in time (right).

345 final time $t = 8750$ days (right, bottom). Note that ADM-LTS automatically
 346 employs fine cells only around the advancing saturation front and that the
 347 active cells in time are only a fraction of them.

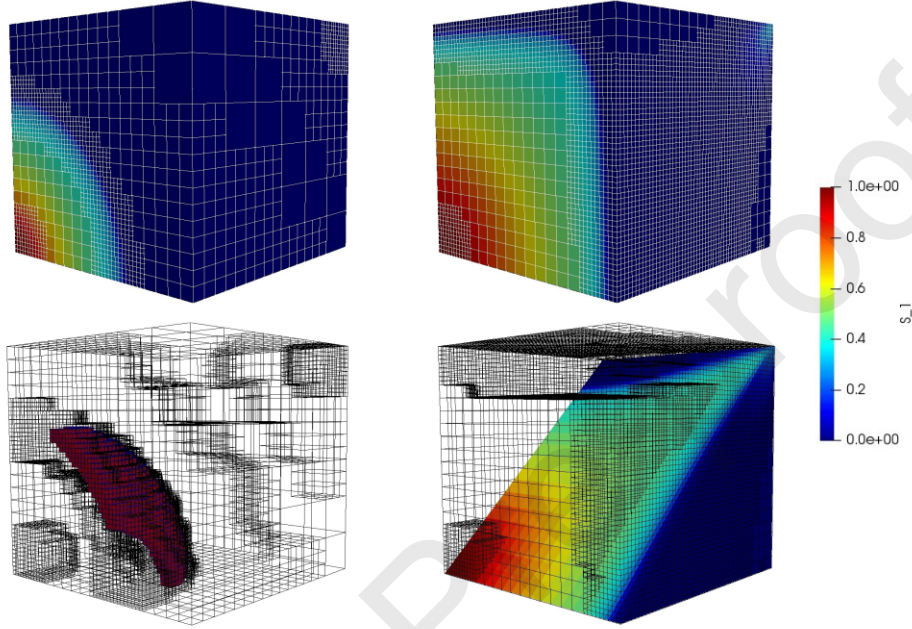


Figure 11: Test case 2 - Saturation profile (top row) at time $t = 1500$ days (left) and at time $t = 8750$ days (right) for the case without gravity. Active cells for the level $l_{ref}=0$ at time $t=1500$ (bottom-left) and saturation profile inside the domain at time $t = 8750$ (bottom-right).

348 Figure 12 shows the saturation maps and the active cells Ω_A^0 at different
 349 times considering the same scenario but introducing a density ratio of ρ_w/ρ_{nw}
 350 $= 5/4$. As expected, the heavier fluid occupies the bottom of the reservoir.

351 Figure 13 shows the total and the mean computational complexity per
 352 local time step for both ADM-LTS and ADM methods. This figure illus-
 353 trates the results with fine time steps, with and without gravity effects. The
 354 transport equation, in the presence of gravitational forces, becomes highly
 355 nonlinear. As a consequence, more Newton iterations are required to con-
 356 verge compared with the case without gravitational effects. Note that, as
 357 shown in Figure 14, the number of ADM-LTS active cells for the two dif-
 358 ferent scenarios is the same during the entire simulation. The number of
 359 active cells increases during the progress of the simulation time, resulting in

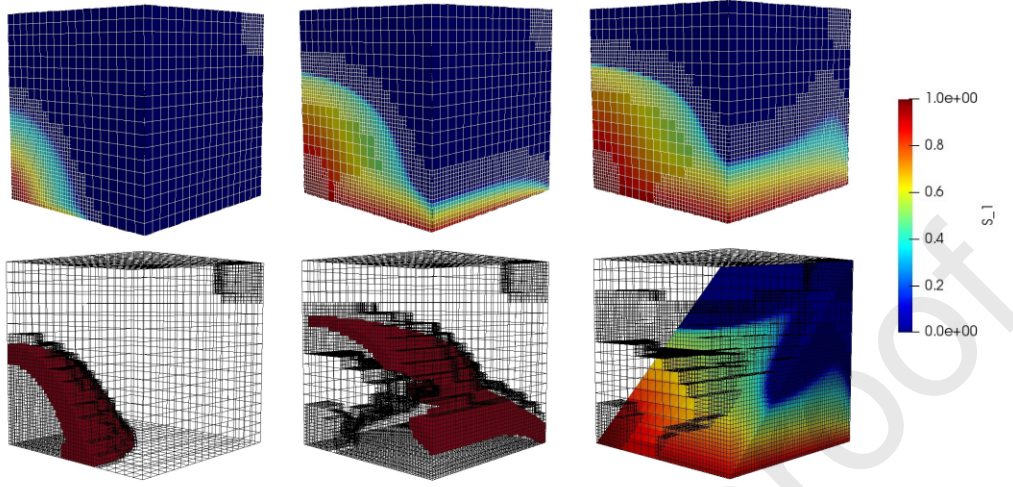


Figure 12: Test case 2 - Saturation profile (top row) at time $t = 1500$ days (left), $t = 6375$ (center) and $t = 8750$ days (right) for the case with gravity. Active cells for the level $l_{ref=0}$ at time $t= 1500$ (bottom-left), active cells for the level $l_{ref=0}$ at time $t= 6375$ (bottom-center) and saturation profile inside the domain at time $t = 8750$ (bottom-right).

360 reduction of the relative errors (Figure 14). The errors of ADM-LTS for the
 361 cases with and without gravity are comparable.

362 4.3. Test case 3: 2D homogeneous reservoir with barrier

363 A 2D homogeneous reservoir with low permeability barriers is considered,
 364 as shown in Fig. 15. The same permeability field was presented in [23]. The
 365 domain dimensions and the physical parameters are the same of the first test
 366 case, the same 99×99 fine scale grid is imposed. The global time step is equal
 367 to 50 [days] and the simulation ends after 100 global time steps ($t = 5000$
 368 days).

369 Simulations are carried out both with the original ADM method em-
 370 ploying a global fine time-step and with ADM-LTS. The coarsening and the
 371 time-refinement criteria tolerances are set to $\epsilon_x = 0.05$ and $\epsilon_t = 0.005$.

372 Figure 16 shows a comparison of the saturation profile and the grid res-
 373 olution for the two different strategies. The original ADM method with a
 374 saturation difference-based coarsening criterion (top row) employs a large
 375 number of fine grid cells wherever saturation gradients are present even if
 376 they are stationary. On the other hand the newly proposed grid resolution
 377 criterion (bottom row) for the ADM-LTS approach uses fine cells only in

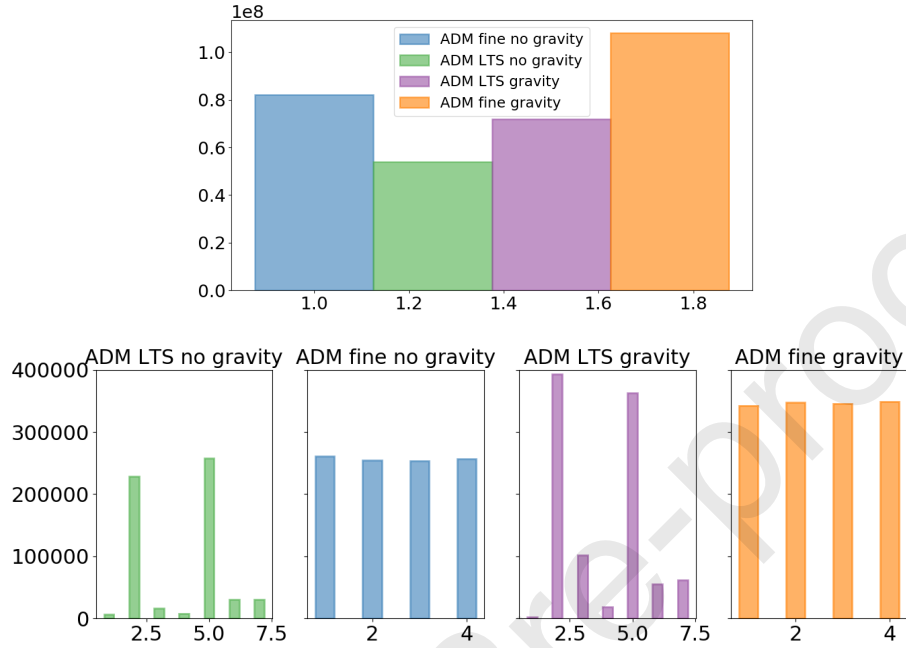


Figure 13: Test case 2 - Computational complexity – total amount of active cells multiplied by the count of Newton iterations for different scenarios (top). Computational complexity history for ADM-LTS and ADM fine-scale time are also presented (bottom).

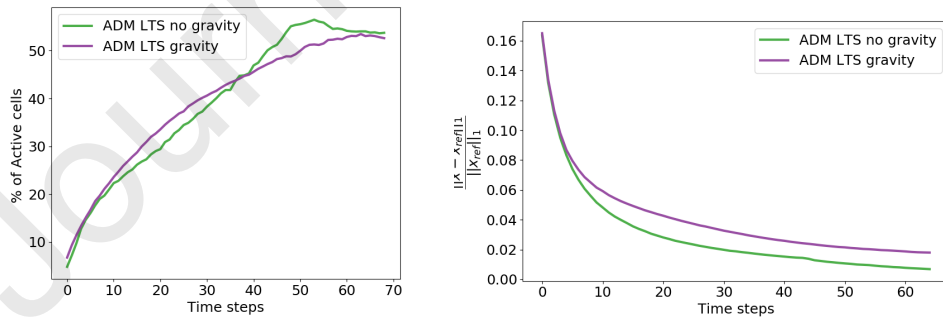


Figure 14: Test case 2 - Number of ADM-LTS active cells for the test cases with and without gravity (left). Also shown (right) are the saturation l^1 -norm errors.

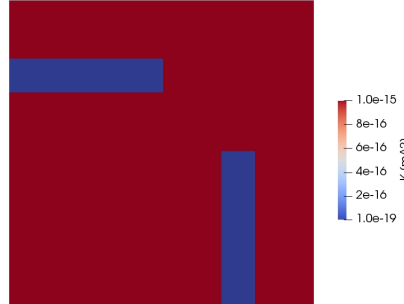


Figure 15: Test case 3 - Absolute permeability field.

378 those regions where the saturation gradient is moving, reducing the number
 379 of active cells.

380 Figure 17 reports the evolution of the active grid cells percentage for the
 381 two different approaches (left) and the evolution of the relative saturation
 382 error in l^1 -norm (right). In the early steps, we can see that the ADM fine
 383 with just the gradient in space criterion approach employs almost the same
 384 number of active grid cells used by the ADM-LTS method. For the ADM
 385 with fine time steps at every small local time step we solve both the flow
 386 and the transport equations, instead for the ADM-LTS approach only the
 387 transport equation is solved for the local steps. This is the reason why in the
 388 first five steps the saturation errors for the ADM-LTS approach are larger
 389 with respect to the ADM fine steps approach. Instead, in the last steps the
 390 errors increase because a lower number of fine grid cells has been used.

391 Figure 18 shows the total complexity (number of active cells multiplied by
 392 the number of Newton iterations) for the ADM with fine steps and the ADM-
 393 LTS approach. Note that the local time steps of ADM-LTS method reduce
 394 the complexity of the system compared to the classical ADM approach.

395 4.4. Test case 4: Heterogeneous reservoir (SPE10 top layer)

396 In this test case a heterogeneous reservoir is considered. The permeability
 397 map is the top layer of the SPE10 test case [24] and it is presented, in
 398 logarithmic scale, in Fig. 19. The size of the reservoir is 2200×600 [m²] and
 399 a 216×54 grid is employed at the finest level. The injector is at the top
 400 left corner and has a constrained pressure 10^7 [Pa]. A producer is, instead,
 401 located at the bottom right corner of the domain with a pressure equal to 0

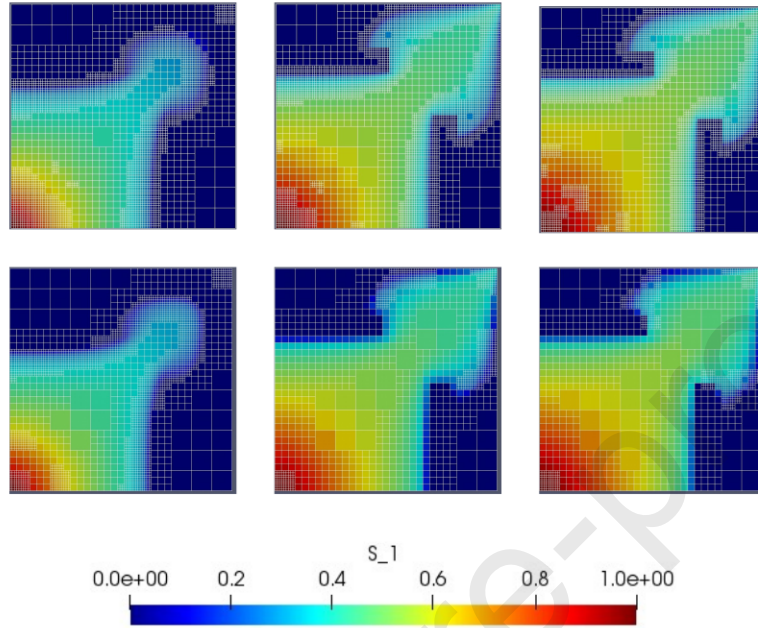


Figure 16: Test case 3 - Saturation profile and ADM grid at different time steps (columns) for ADM with coarse time steps and classical ADM grid resolution (first row) and for ADM-LTS method with the new ADM grid resolution (second row).

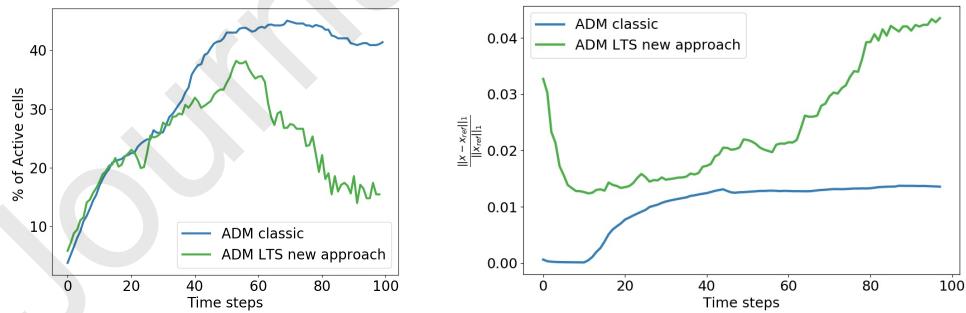


Figure 17: Test case 3 - number of active cells employed in ADM with fine grid in time and ADM-LTS simulations expressed as percentage of fine grid cells (left) and the saturation relative errors in l^1 -norm for the ADM fine and ADM-LTS method (right).

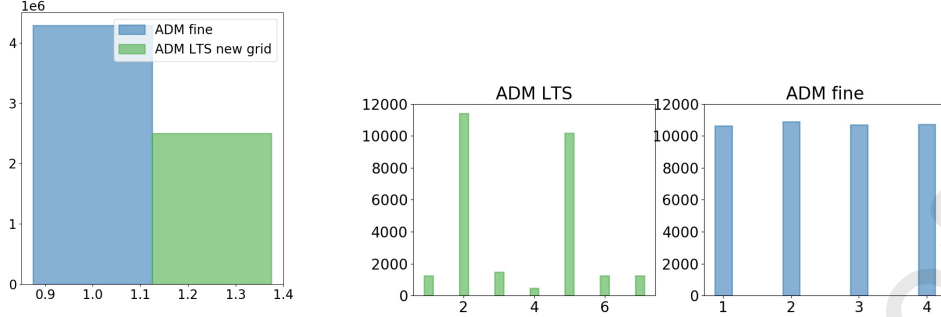


Figure 18: Test case 3 - Total amount of active cells multiplied by number of Newton iterations (left) and computational complexity history at each local times step within a global step (right) for the ADM with fine time steps approach and for the ADM-LTS method.

402 [Pa]. The porosity of the reservoir ϕ is equal to 0.2. The viscosity for the
 403 wetting phase is 10^{-5} [Pa · s], whereas, for the non-wetting phase, is 10^{-4}
 404 [Pa · s]. The coarsening ratio for the space grid is equal to 2 as well as the
 405 time refining ratio. The error tolerance for the time estimator is equal to
 5×10^{-2} .

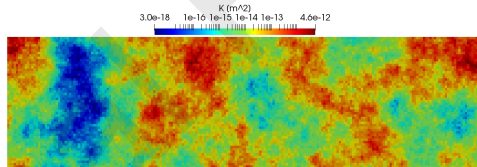


Figure 19: Test case 4 - Natural logarithm of the permeability.

406

407 Figure 20 reports the saturation map and the ADM grid for different
 408 threshold values of the ADM grid resolution criterion using the classical ADM
 409 approach with fine time steps, and the ADM-LTS approach with the new grid
 410 resolution strategy. The classical approach uses, for small threshold values,
 411 a large number of fine grid cells. If we relax the threshold parameter the
 412 method is not able to capture the fronts. Thanks to the new ADM-LTS
 413 approach, the method is able to apply the fine grid cells only where the front
 414 is moving fast (high permeability regions).

415 Figure 21 shows the active cells in time at the finest level $l_{ref} = 2$ for
 416 different global time steps. The method recomputes the solution with small

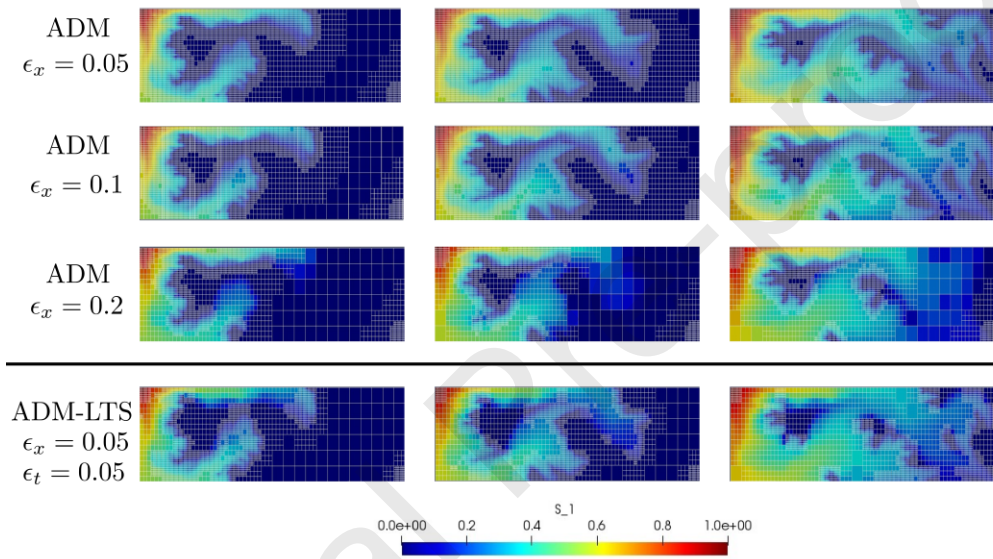


Figure 20: Test case 4 - Saturation map and ADM grid for the ADM with fine time step approach with classical grid criterion for different values of the threshold $\epsilon_x = 0.05, 0.1, 0.2$ (row 1, 2, and 3) and for the ADM-LTS method with the new grid criterion $\epsilon_x = 0.05$ and $\epsilon_t = 0.05$ (row 4) at time $t = 1200$ days (first column), $t = 15000$ days (second column) and $t = 20000$ days (third column).

417 time steps only for a few percentage of cells where the front crosses high
 418 permeability regions. In fact, in the last snapshot, the saturation profile is
 almost developed everywhere and so, the set of active cells is very small.

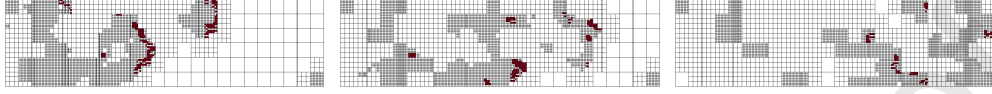


Figure 21: Test case 4 - Active cells for the refinement in time, at time $t = 1200$ days (left), $t = 15000$ days (center) and $t = 20000$ days (right).

419

420 In Figure 22 we compare the number of active cells and the saturation
 421 errors for the different simulations. Using the classical ADM approach with
 422 small values of the tolerance a lot of active grid cells are employed giving
 423 very small errors. The classical ADM approach with larger tolerance value
 424 and the ADM-LTS method are comparable in terms of active cells during all
 425 the simulation but the ADM-LTS approach gives better results in term of
 426 errors.

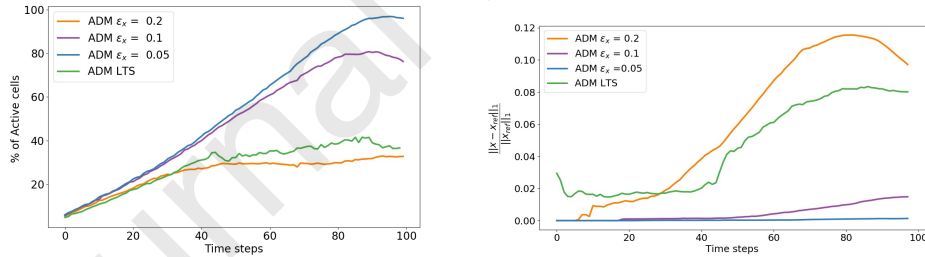


Figure 22: Test case 4 - Number of active cells expressed as percentage of fine grid cells (left) and saturation relative errors in l^1 -norm (right) for the ADM with fine grid in time with different values of the threshold and for the ADM-LTS simulation.

427 Figure 18 reports the complexity of the four simulations. The ADM
 428 approach with fine grid in time and small threshold values is really expensive.
 429 The ADM-LTS approach is comparable to the ADM with fine time step
 430 approach and large value of ϵ_x but, as shown previously, the solution of the
 431 classic ADM, in this case, is not as accurate.

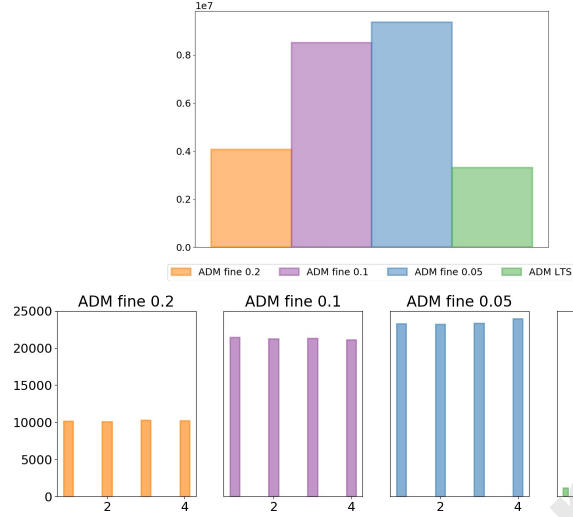


Figure 23: Test case 4 - Total amount of active cells multiplied by number of Newton iterations (top) and computational complexity history at each local times step within a global step (bottom) for the ADM approach.

4.5. Test case 5: Heterogeneous reservoir (SPE10 bottom layer)

The permeability of SPE10 bottom layer is used for this test case, as show in Figure 24. This layer, with respect to the previous case has higher contrasts and more a channelized distribution.

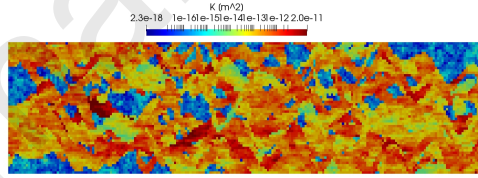


Figure 24: Test case 5 - Natural logarithm of the permeability.

435

436 The global time step is equal to 10 days and the simulation ends after
 437 50 global time steps. The input parameters for the wells and the physical
 438 properties are identical to Test Case 4.

439 The top 2 rows of Fig. 25 show the saturation distribution at simula-
 440 tion time of 150, 250 and 350 days obtained with $\epsilon_x = 0.15$ and $\epsilon_x = 0.2$,
 441 respectively. The bottom rows, instead, show the saturation map, at the
 442 same simulations times, obtained by employing the ADM-LTS method with

443 $\epsilon_x = 0.05$ and $\epsilon_t = 5 \times 10^{-2}$ and $\epsilon_t = 5 \times 10^{-3}$. The classic ADM ap-
 444 proach employs a large number of active cell during the simulation, instead
 445 the ADM-LTS method is able to select a fine scale grid only where the fronts
 446 are moving.

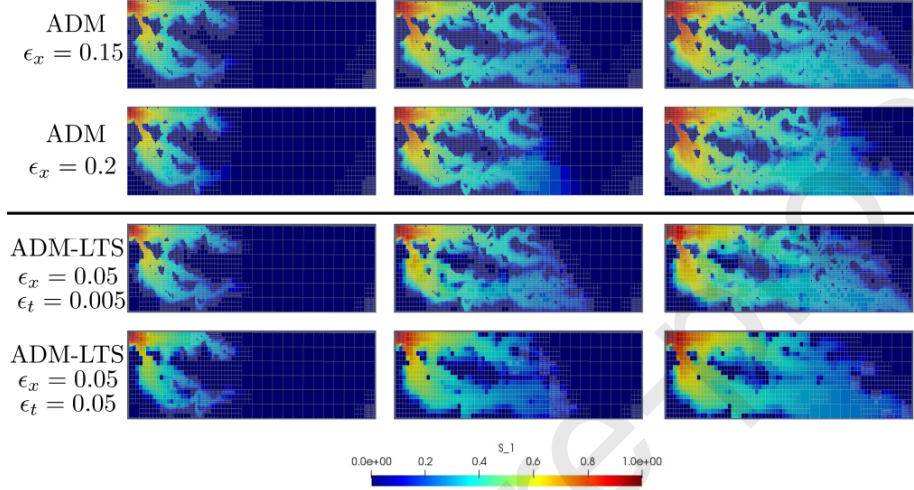


Figure 25: Test case 5 - Saturation map and ADM grid at 150, 250 and 350 days for the ADM approach with fine time steps and the ADM-LTS approach.

447 Figure 26 shows the active cells in time for $l_{ref} = 2$ at time 150, 250
 448 and 350 days. As expected, for smaller value of the threshold more cells are
 449 involved in the refinement step.

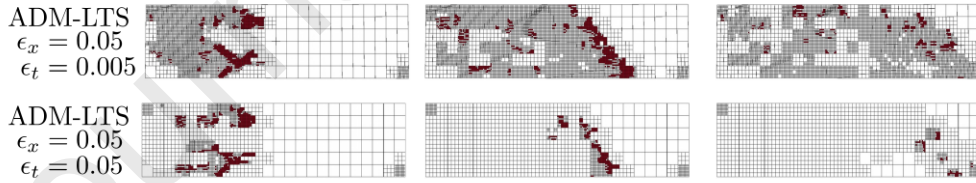


Figure 26: Test case 5 - Active cells for the refinement level $l_{ref} = 2$, at 150 (left), 250 (center) and 350 (right) days for the two threshold values.

450 The history of the percentage of active cells employed by the different
 451 simulation strategies for the various tolerances is shown in Fig. 27 (left),
 452 along with the l^1 norm of the saturation error (right). For both the ADM-
 453 LTS tolerance values less active cells are involved respect to the classical

454 ADM approach. Since a smaller number of cells is employed, the saturation
 455 errors are higher but still of the same order of magnitude.

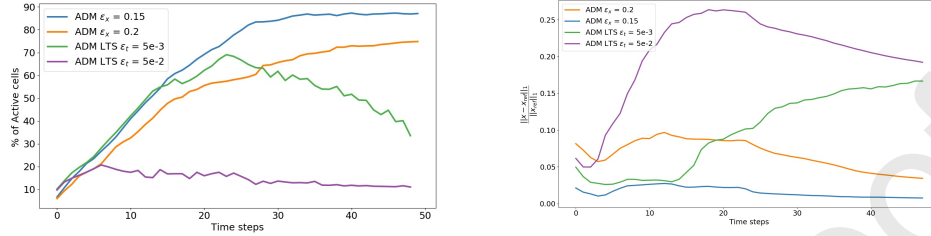


Figure 27: Test case 5 - Number of active cells expressed as percentage of fine grid cells (left) and saturation relative errors in l^1 -norm (right) for the ADM with fine grid in time and for the ADM-LTS simulations.

456 Figure 28 reports the complexity of the four simulations for different
 457 tolerance values.

458 4.6. Test case 6: Heterogeneous reservoirs with different layering orienta- 459 tions.

460 A $500 \times 500 \text{ m}^2$ 2D reservoir is considered on which a 99×99 grid is im-
 461 posed. The fluid properties, the location of the wells and their constraints are
 462 the same as in the previous test cases. Five sets of permeability fields, with
 463 different layering orientation and created using sequential Gaussian simula-
 464 tions with spherical variogram and dimensionless correlation lengths 0.5 and
 465 0.02 as proposed in [25], are considered. Each set consists of 20 statistically
 466 identical realizations.

467 Figure 29 shows one realization for each set. Injection of the wetting
 468 phase, for 560 days, is simulated for each realization. Simulations are run
 469 with the ADM-LTS method. For all runs, the spatial coarsening criterion
 470 tolerance is $\epsilon_x = 0.008$. Two different values are instead considered for the
 471 time-based criterion tolerance, ϵ_t : 5×10^{-2} and 5×10^{-3} .

472 Figure 30 shows a comparison, for one permeability realization of each
 473 set, of the saturation map at the end of the simulation obtained with fine-
 474 scale (time and space) simulation (top row), ADM-LTS employing a fixed
 475 refined time-step.

476 Figure 31 displays the active cells in time for the last refinement level of
 477 the last global time step. As expected, using a bigger value of the tolerance
 478 for the time error estimator, just few cells need to be computed with small

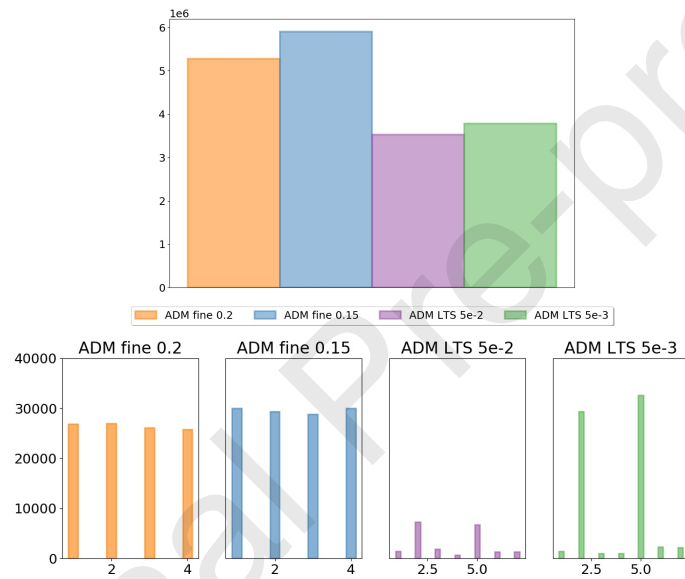


Figure 28: Test case 5 - Total amount of active cells multiplied by number of Newton iterations (top) and computational complexity history at each local times step within a global step (bottom) for the ADM approach.

479 time steps. Moreover, the space grid changes and allows to use coarser grid
 480 cells.

481 Figure 32 represents the mean and the standard deviations of the complex-
 482 ity for the ADM-LTS method using the two different time-based criterion
 483 tolerances and for the solution computed with the fine grid resolution both
 484 in space and in time. Note that the y-axis scale for the two pictures are
 485 different.

486 Figure 33 shows the mean and the standard deviations of the saturation
 487 errors respect to the reference solution for the ADM-LTS method using the
 488 two different time-based criterion tolerances. From these studies, one can
 489 conclude that the ADM-LTS performs robustly when several equiprobable
 490 realizations are considered. In other words, the error and computational
 491 complexities for all 20 realizations are not much different compared with the
 492 average values.

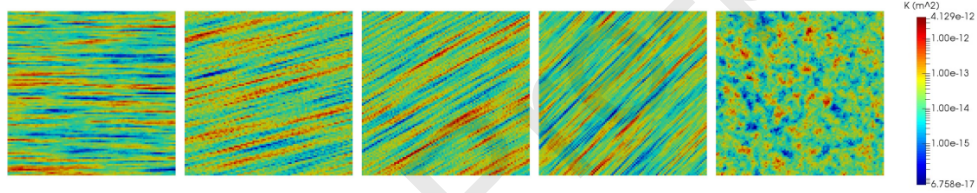


Figure 29: Test case 6 - One of the 20 realization of each of the 5 sets of permeability fields with different angles (0 deg, 15 deg, 30 deg, 45 deg and patchy from left to right).

493 4.7. Test case 7: Capillary forces.

494 A $500 \times 500[\text{m}^2]$ heterogeneous reservoir is considered. The fine-scale grid
 495 contains 99×99 cells. The phase viscosity values are $\mu_w = 1e - 4[\text{Pa} \cdot \text{s}]$ and
 496 $\mu_{nw} = 1e - 3[\text{Pa} \cdot \text{s}]$. Five pressure-constrained wells are present, as shown in
 497 Figure 34 along with the heterogeneous permeability field. The well locations
 498 and the pressure values are presented in Table 1.

499 The simulation is run until 2500[days] after injection is reached. A time
 500 step size equal to 10[days] is used. The ADM-LTS employs a time refining
 501 ratio of $\eta = 2$ and a space coarsening ratio of 3. The user-defined tolerances
 502 are set as $\epsilon_x = 0.25$ and $\epsilon_t = 1 \times 10^{-2}$. The same capillary pressure function
 503 as in [12, 26] is considered, i.e.,

$$P_c = \sigma \cos(\theta) \sqrt{\frac{\phi}{K}} J(S), \quad (25)$$

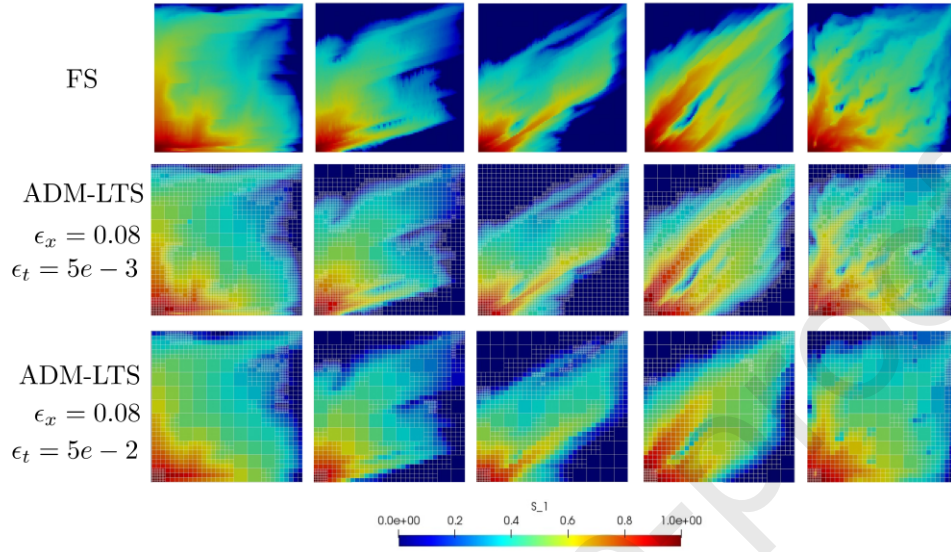


Figure 30: Test case 6 - Comparison of the saturation profile, for one realization of each set of permeability fields at time $t = 560$ days. Two different threshold values for the time error estimator are employed for the ADM-LTS simulation (center row and bottom row), the fine scale solution are also shown (top row).

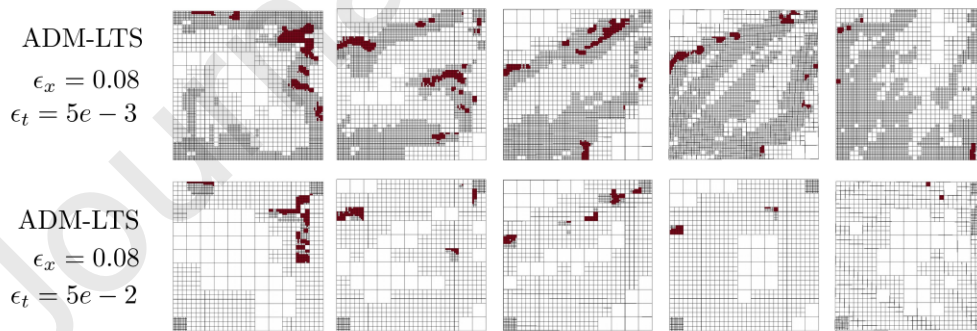


Figure 31: Test case 6 - Active calls at the last refinement level for the last global time step using two different threshold values for the error estimator in time.

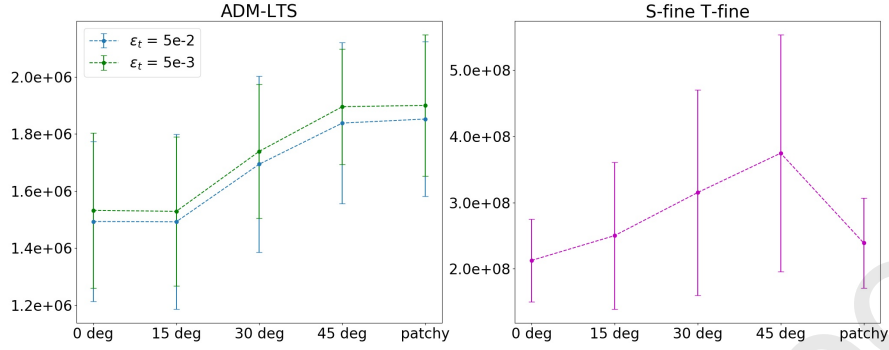


Figure 32: Test case 6 - Mean and standard deviation of complexity over 20 realization for the ADM-LTS method (left) and for the reference solution computed with fine grid resolution both in space and time (right).

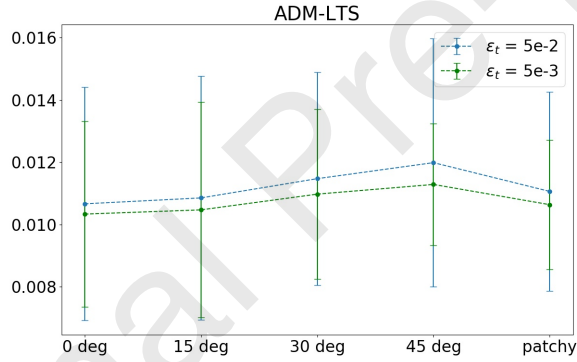


Figure 33: Test case 6 - Mean and standard deviation errors of the saturation errors over 20 realization for the ADM-LTS method with different time threshold values respect to the reference solution $E_S = \text{mean}_{t=1}^{N_t} (\text{mean}|S_f(t) - S(t)|)$.

Well	x	y	Pressure [bar]
Prod (W1)	1	1	120
Prod (W2)	99	1	120
Prod (W3)	99	99	100
Prod (W4)	1	99	100
Inj (W5)	50	50	150

Table 1: Test case 7 - Wells coordinates and constraints.

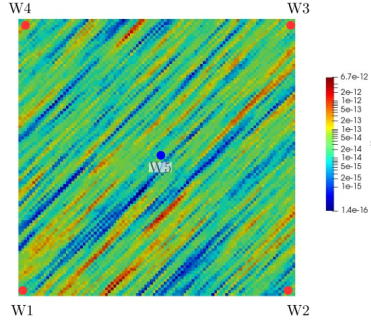


Figure 34: Test case 7 - Base 10 logarithm of the permeability field.

504 where

$$J(S) = 0.05 \left(\frac{1}{S} \right)^{-0.5}. \quad (26)$$

505 Here, S is the saturation of the wetting phase, $\sigma = 4.361 \times 10^{-2} [\text{Pa} \cdot \text{m}]$
 506 the surface tension and $\theta = 0$ the contact angle. Figure 35 compares the
 507 reference solution (fine-scale) and the ADM-LTS approach with and without
 508 including the effect of capillary pressure. The ADM-LTS approach, as shown
 509 in Figure 36, in presence of capillary pressure employs more active cells,
 510 since the saturation map is more complex compared with the case without
 511 capillary effects. In this test case, the complex physics induced by capillary
 512 heterogeneity is present in almost the entire computational domain. There-
 513 fore, the advancing saturation front is present in a large sub-region of the
 514 domain. As the result, in this case, 70% of the active cells are used to obtain
 515 accurate solutions. Figure 36 shows the errors in l^1 norm for the ADM-LTS
 516 method with and without capillary effects. After the global time step 150,
 517 the saturation error increases due to coarsening some fine cells. Then after
 518 200 days, the error is stabilized.

519 5. Conclusions

520 A dynamic local space-time stepping scheme for transport in porous me-
 521 dia (ADM-LTS) was devised and integrated within the sequentially-coupled
 522 multiphase flow-transport system. The studied coupled multiphase flow pro-
 523 cesses observe pressure and velocity change at every time step. The ADM-
 524 LTS method operates in two stages: first the solution is obtained at the

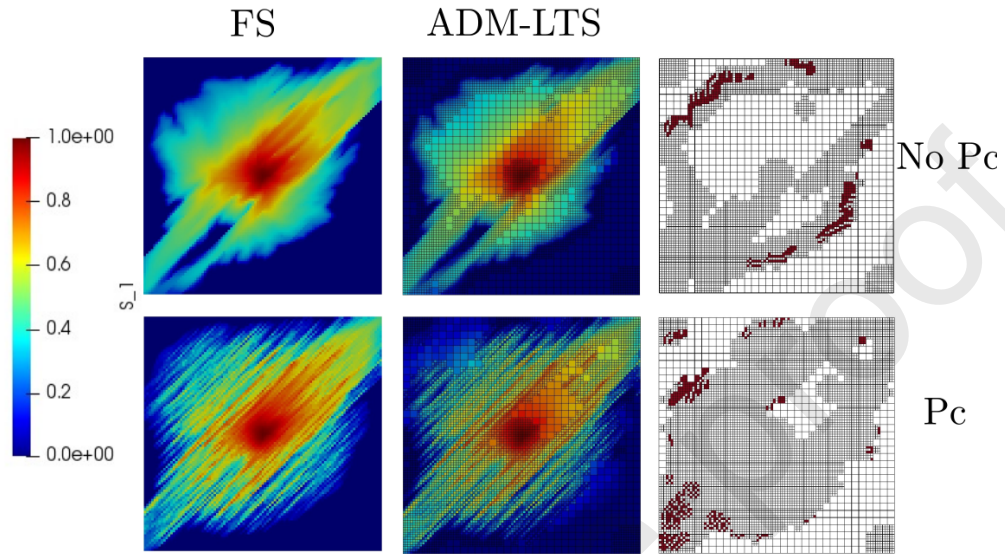


Figure 35: Test case 7 - Reference solutions (left) and ADM-LTS saturation maps (right) without (top) and with (bottom) capillary heterogeneity effects.

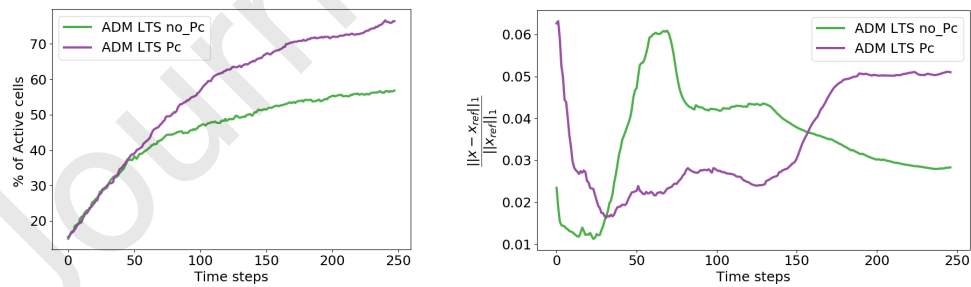


Figure 36: Test case 7 - Number of active cells expressed as percentage of fine grid cells (left) and saturation relative errors in l^1 -norm (right) for the ADM-LTS simulations.

525 coarsest space-time grid. Then this initial solution is improved by impos-
526 ing an adaptive multi-resolution grid in space and time. The resolution of
527 the space-time grid is defined based on an error criteria, with user-defined
528 threshold values. This strategy also guarantees local mass conservation.

529 Compared with the classical ADM approach, the ADM-LTS method em-
530 ploys coarse grids where high saturation gradients exist, but the phase veloc-
531 ity is nearly zero. This happens when the saturation front faces impermeable
532 zones or barriers. The ADM-LTS grid resolution is decided implicitly by the
533 mentioned two-stage strategy, where initially the coarsest space-time grid is
534 used everywhere. Then, based on the introduced error criteria, the transport
535 solution is locally improved with a multirate multilevel strategy on an adap-
536 tive space-time grid. This method is found promising to reduce the size of
537 the system in the nonlinear loop without loss of accuracy.

538 Several numerical test cases with challenging transport physics were con-
539 sidered. Results showed that the ADM-LTS is promising for real-field ap-
540 plications. The research simulator (with all numerical test cases) is made
541 available to the public (<https://gitlab.com/darsim2simulator>).

542 Future work include development of enhanced prolongation operators to
543 further improve the saturation quality at coarser levels (specially for slow-
544 moving fronts). Another ongoing work is the implementation of ADM-LTS
545 in the DARSim1 C++ research simulator for large-scale 3D test cases.

546 Acknowledgements

547 Hadi Hajibeygi was funded by the 2019 Dutch National Science Founda-
548 tion (NWO) grant, under Vidi scheme, with award number of 17509 (Project
549 ADMIRE). Matteo Cusini was sponsored by the auspices of the U.S. Depart-
550 ment of Energy by Lawrence Livermore National Laboratory (LLNL) under
551 Contract DE-AC52-07NA27344. Authors thank Delft Advanced Reservoir
552 Simulation (DARSim) research group members for the fruitful discussions
553 during the development of the ADM-LTS method.

554 References

- 555 [1] D. R. Brouwer, J. D. Jansen, Dynamic optimization of water flooding
556 with smart wells using optimal control theory, SPE journal 4 (2004)
557 391–402. doi:<https://doi.org/10.2118/78278-MS>.

- 558 [2] R. J. de Moraes, J. R. Rodrigues, H. Hajibeygi, J. D. Jansen,
559 Multiscale gradient computation for flow in heterogeneous porous
560 media, *Journal of Computational Physics* 336 (2017) 644 – 663.
561 doi:<https://doi.org/10.1016/j.jcp.2017.02.024>.
- 562 [3] M. Cusini, R. Gielisse, H. Groot, C. van Kruijsdijk, H. Hajibeygi, Incom-
563 plete mixing in porous media: Todd-longstaff upscaling approach versus
564 a dynamic local grid refinement method, *Computational Geosciences*
565 23 (2) (2019) 373–397. doi:10.1007/s10596-018-9802-0.
- 566 [4] T. Y. Hou, X.-H. Wu, A multiscale finite element method for elliptic
567 problems in composite materials and porous media, *Journal of compu-
568 tational physics* 134 (1) (1997) 169–189.
- 569 [5] P. Jenny, S. Lee, H. Tchelepi, Multi-scale finite-volume method for el-
570 liptic problems in subsurface flow simulation, *Journal of Computational
571 Physics* 187 (1) (2003) 47 – 67.
- 572 [6] H. Hajibeygi, G. Bonfigli, M. A. Hesse, P. Jenny, Iterative multiscale
573 finite-volume method, *Journal of Computational Physics* 227 (19) (2008)
574 8604 – 8621.
- 575 [7] H. Zhou, H. A. Tchelepi, et al., Two-stage algebraic multiscale linear
576 solver for highly heterogeneous reservoir models, *SPE Journal* 17 (02)
577 (2012) 523–539.
- 578 [8] O. Møyner, K.-A. Lie, A multiscale restriction-smoothed basis
579 method for high contrast porous media represented on unstruc-
580 tured grids, *Journal of Computational Physics* 304 (2016) 46 – 71.
581 doi:<https://doi.org/10.1016/j.jcp.2015.10.010>.
- 582 [9] M. J. Berger, J. Olinger, Adaptive mesh refinement for hyperbolic partial
583 differential equations, *Journal of Computational Physics* 53 (3) (1984)
584 484 – 512. doi:[https://doi.org/10.1016/0021-9991\(84\)90073-1](https://doi.org/10.1016/0021-9991(84)90073-1).
585 URL <http://www.sciencedirect.com/science/article/pii/0021999184900731>
- 586 [10] B. Faigle, R. Helmig, I. Aavatsmark, B. Flemisch, Efficient multiphysics
587 modelling with adaptive grid refinement using a mpfa method, *Compu-
588 tational Geosciences* 18 (5) (2014) 625–636. doi:10.1007/s10596-014-
589 9407-1.

- 590 [11] M. Cusini, C. van Kruijsdijk, H. Hajibeygi, Algebraic dynamic multi-
591 level (adm) method for fully implicit simulations of multiphase flow in
592 porous media, *Journal of Computational Physics* 314 (2016) 60 – 79.
593 doi:<https://doi.org/10.1016/j.jcp.2016.03.007>.
- 594 [12] M. Cusini, B. Fryer, C. van Kruijsdijk, H. Hajibeygi, Algebraic
595 dynamic multilevel method for compositional flow in heterogeneous
596 porous media, *Journal of Computational Physics* 354 (2018) 593 – 612.
597 doi:<https://doi.org/10.1016/j.jcp.2017.10.052>.
- 598 [13] J. Andrus, Numerical solution of systems of ordinary differential equa-
599 tions separated into subsystems, *SIAM Journal of Numerical Analysis*
600 16 (1979) 605–611.
- 601 [14] V. Savcenco, W. Hundsdorfer, J. Verwer, A multirate time stepping
602 strategy for stiff ordinary differential equations, *BIT Numerical Mathe-*
603 *matics* 47 (2007) 137–155.
- 604 [15] L. Delpopolo Carciopolo, L. Bonaventura, A. Scotti, L. Formaggia, A
605 conservative implicit multirate method for hyperbolic problems, *Com-*
606 *putational Geosciences* 23 (4) (2019) 647–664. doi:10.1007/s10596-018-
607 9764-2.
- 608 [16] L. Delpopolo Carciopolo, L. Formaggia, S. Anna, H. Hajibeygi, Con-
609 servative multirate multiscale simulation of multiphase flow in hetero-
610 geneous porous media.
- 611 [17] P. Jenny, Time adaptive conservative finite volume method, submitted.
- 612 [18] G. W. Thomas, D. H. Thurnau, Reservoir simulation using an adaptive
613 implicit method, *Society of Petroleum Engineers Journal* 23 (05) (1983)
614 759–768. doi:10.2118/10120-PA.
- 615 [19] D. A. Collins, L. X. Nghiem, Y.-K. Li, J. E. Grabonstotter, An effi-
616 cient approach to adaptive- implicit compositional simulation with an
617 equation of state, *SPE Reservoir Engineering* 7 (02) (1992) 259–264.
618 doi:10.2118/15133-PA.
- 619 [20] J. Maes, A. Moncorgé, H. Tchelepi, Thermal adaptive implicit method:
620 Time step selection, *Journal of Petroleum Science and Engineering* 106
621 (2013) 34 – 45. doi:<https://doi.org/10.1016/j.petrol.2013.03.019>.

- 622 [21] R. Helmig, *Multiphase Flow and Transport Processes in the Subsur-*
623 *face: A Contribution to the Modeling of Hydrosystems*, Environmental
624 engineering, Springer, 1997.
- 625 [22] Z. Chen, G. Huan, Y. Ma, *Computational methods for multiphase flows*
626 *in porous media*, Vol. 2, Siam, 2006.
- 627 [23] M. Cusini, H. Hajibeygi, Algebraic dynamic multilevel (adm) method for
628 simulations of multiphase flow with an adaptive saturation interpolator,
629 in: *ECMOR XVI-16th European Conference on the Mathematics of Oil*
630 *Recovery*, 2018.
- 631 [24] M. Christie, M. Blunt, Tenth SPE comparative solution project: A com-
632 parison of upscaling techniques, *SPE Reservoir Simulation Symposium*
633 11-14 February, 2001.
- 634 [25] N. Remy, A. Boucher, J. Wu, *Applied geostatistics with SGeMS: a user's*
635 *guide*, Cambridge University Press, 2009.
- 636 [26] B. Li, S. M. Benson, Influence of small-scale heterogeneity on upward
637 co2 plume migration in storage aquifers, *Advances in Water Resources* 83
638 (2015) 389 – 404. doi:<https://doi.org/10.1016/j.advwatres.2015.07.010>.

Declaration of interests

The authors declare that they have no known competing financial interests or personal relationships that could have appeared to influence the work reported in this paper.

The authors declare the following financial interests/personal relationships which may be considered as potential competing interests:

Journal Pre-proof

Conflict of Interest and Authorship Conformation Form

Please check the following as appropriate:

- All authors have participated in (a) conception and design, or analysis and interpretation of the data; (b) drafting the article or revising it critically for important intellectual content; and (c) approval of the final version.
- This manuscript has not been submitted to, nor is under review at, another journal or other publishing venue.
- The authors have no affiliation with any organization with a direct or indirect financial interest in the subject matter discussed in the manuscript
- The following authors have affiliations with organizations with direct or indirect financial interest in the subject matter discussed in the manuscript:

Author's name

Affiliation

Author's name	Affiliation
Ludovica Delpopolo Carciopolo	Politecnico di Milano
Matteo Cusini	Livermore National Laboratory
Luca Formaggia	Politecnico di Milano
Hadi Hajibeygi	TU Delft